

Raman Imaging and Kelvin Probe Microscopy for the Examination of the Heterogeneity of Doping in Polycrystalline Boron-Doped Diamond Electrodes

Sabine Szunerits,^{*,†} Michel Mermoux,^{*,†} Alexandre Crisci,[†] Bernadette Marcus,[†] Pierre Bouvier,[†] Didier Delabouglise,[†] Jean-Pierre Petit,[†] Sebastian Janel,^{‡,§} Rabah Boukherroub,^{‡,§} and Lilin Tay^{||}

Laboratoire d'Electrochimie et de Physicochimie des Matériaux et des Interfaces, CNRS-INPG-UJF, 1130 rue de la piscine, BP 75, 38402 St. Martin d'Hères Cedex, France, Institut de Recherche Interdisciplinaire (IRI), FRE 2963, France, Institut d'Electronique, de Microélectronique et de Nanotechnologie (IEMN), CNRS-8520, Cité Scientifique, Avenue Poincaré - BP 60069, 59652 Villeneuve d'Ascq, France, and National Research Council, IMS, 1200 Montreal Road, Ottawa, Ontario K1A 0R6 Canada

Received: July 13, 2006; In Final Form: September 8, 2006

The issue of the heterogeneity of boron doping in microcrystalline diamond films was addressed by four different methods: micro-Raman spectroscopy and Raman imaging, Kelvin probe force microscopy, conducting atomic force microscopy, and scanning electrochemical microscopy. The samples were commercially available films from Windsor Scientific, with an average boron concentration of about $5 \times 10^{20} \text{ cm}^{-3}$. In agreement with previous works, all of the methods showed that the boron uptake was nonuniform across the surface of the electrode. Two different types of regions were evidenced, with metallic or semiconducting properties that were characterized with different types of Raman spectra. The line shape of these spectra was strongly dependent on the excitation wavelength. Local variations in electroactivity were evidenced by the SECM curves, which are related to the electronic properties of the individual grains, which, in turn, are governed by the boron content of the individual crystallites. In this study, two different micro-Raman imaging techniques were used that reveal the grain structure of the films: the images constructed from the diamond line intensity perfectly reproduced the optical image obtained by illuminating the sample in reflection. The method also allows detection of the presence of nondiamond carbon, especially in the metallic parts of the samples. Other spectral features (intensity of the boron-related broad lines, as well as the frequency and width of the diamond line) were used to construct images. In every case, the grain structure of the film was revealed, as well as twinning within individual crystallites. All approaches revealed that no enhanced doping or boron depletion occurred at the grain boundaries.

1. Introduction

Boron-doped diamond (BDD) thin films have gained remarkable interest because of their specific physical properties. BDD electrodes show excellent mechanical properties, extreme chemical stability, good biocompatibility, good electrical conductivity, low background current densities, and a large potential window in aqueous electrolytes (about -1.35 to 2.3 V vs NHE).^{1,2} As a result, this new electrode material has found use in electroanalysis,³ wastewater purification,⁴ and biomedical applications.^{5–8} Polycrystalline BDD is generally produced by a variety of chemical vapor deposition (CVD) techniques. The boron dopant is added to the source gas ($0.3\text{--}1\%$ CH_4 in H_2), often in the form of diborane (B_2H_6), at concentrations varying between 1 and 10000 ppm. Depending on the growth conditions used, the properties of the diamond interface, such as the boron concentration, the morphology and size of the individual grains,

and the ratio between nondiamond and diamond carbon, can be varied in a wide range.

Although the above properties make BDD electrodes an attractive interface, many factors influence their electrochemical behavior. The most influential are (a) the dopant concentration and resulting dopant density, (b) the surface termination, (c) nondiamond carbon impurities (e.g., sp^2 inclusions), (d) crystallographic orientation, and (e) fraction of grain boundaries.

The dopant concentration probably has the greatest influence on the electrical and electrochemical properties of BDD electrodes. Schematically, for doping concentrations below $\sim 10^{19} \text{ cm}^{-3}$, the apparent thermal activation energy equals the ionization energy $E_{\text{a,opt}} = 0.36 \text{ eV}$ found in optical experiments. Because of the high bonding energy of the boron acceptors, only a small fraction ($\sim 0.2\%$) of them are ionized at room temperature. Current conduction is a result of compensation-dependent band conduction. In the intermediate boron concentration range [10^{19} –(2×10^{20}) cm^{-3}], current conduction is dominated by nearest-neighbor hopping, and the hopping-related activation energy depends on the boron concentration. At still higher boron concentrations, “metallic” conduction is observed, with room-temperature conductivities on the order of $10^2 \Omega^{-1} \text{ cm}^{-1}$.¹⁰ In this concentration range, the carrier concentration is comparable to the solid-state boron concentration. This phe-

* To whom correspondence should be addressed. E-mail: sabine.szunerits@lepmi.inpg.fr (S.S.), michel.mermoux@lepmi.inpg.fr (M.M.). Phone: +33-4 76.82.65.52 (S.S.), +33-4 76.82.33.12 (M.M.). Fax: 33-4 76.82.66.30 (S.S.), 33-4 76.82.66.30 (M.M.).

[†] Laboratoire d'Electrochimie et de Physicochimie des Matériaux et des Interfaces.

[‡] Institut de Recherche Interdisciplinaire (IRI).

[§] Institut d'Electronique, de Microélectronique et de Nanotechnologie (IEMN).

^{||} National Research Council.

nomenon is related to the decrease in the activation energy with increasing boron concentration. Boron atoms can also accumulate at grain boundaries. Grain boundary effects were reported by Holt et al. using C-AFM and SECM on very rough surfaces.⁹ However, the coating at the tip apex can quickly wear at such surfaces, resulting in artifacts particularly at steps and edges where the side of the metal-coated tip makes contact with the surface.

The surface termination is a second important parameter for BDD electrodes. Because the deposition of diamond films is undertaken in a reductive medium (hydrogen plasma), the as-deposited diamond surface is hydrogen-terminated. However, this surface can be easily oxidized by a number of methods. The presence of oxygen on the diamond surface has a significant influence on the chemical reactivity,^{11,12} electrical conductivity,^{1,2,13,14} and electron affinity.¹⁵ Various conditions for diamond oxidation are reported in the literature, including thermal,^{16,17} plasma,^{18,19} photochemical,²⁰ electrochemical,^{21–23} and singlet oxygen²⁴ techniques. Thermal oxidation of hydrogen-terminated diamond under various conditions showed a final surface composition dominated by ether (C–O–C) and carbonyl (C=O) groups.¹⁷ Although hydrogen termination has been found to promote the surface conductivity of intrinsic diamond,²⁵ for heavily doped films, the conversion from hydrogen to oxygen surface termination does not significantly change the surface conductivity.²⁶

The third factor is the fraction of sp²-bonded carbon often present within the grain boundaries or defect sites, which can show activity differing from the surrounding BDD material.²⁷

All of these factors add to the heterogeneity of the surface of polycrystalline BDD. An additional complication is that boron uptake is known to depend on the crystallographic surface.^{28,29} Boron is more readily included into (111) facets than (100) sectors. Consequently, different grains can show different electrical and electrochemical behaviors ranging from semi-conducting to metallic characteristics because of different boron uptakes.

Different approaches have been used by various research groups to image the spatial distribution of the boron concentration and the variation in electroactivity at the surface of highly doped polycrystalline diamond. Honda et al. used electrogenerated chemiluminescence (ECL) generated by the reaction of Ru(bpy)₃²⁺ and tripropylamine to show the location and size of individual active regions.³⁰ The ECL intensities for (100)-oriented growth sectors were much lower than those for other growth sectors and remained at about 50% of those for (111) sectors. Raman imaging was used by the same group and showed that, by mapping the intensities of the one-phonon diamond line, the regions of maximum line intensity correspond to (100)-oriented microcrystallites. Confocal micro-Raman imaging was also used by our group to investigate the structural and, to some extent, chemical inhomogeneities that exist in a high-quality, free-standing, polished, optically transparent boron-doped CVD diamond disk.³¹ Steeds et al. used transmission electron microscopy (TEM) as well as photoluminescence and micro-SIMS to investigate the nature of the inhomogeneities on boron-doped CVD diamond films.^{32–34} TEM showed that grains in thick polycrystalline CVD diamond form clusters with a common growth direction. The individual grains within a cluster are related by various twinning operations, which are characteristic of columnar CVD growth and do not depend on boron doping. Micro-SIMS clearly indicated the nonuniform introduction of boron into diamond samples, but it was unable to provide quantitative information.³² Bard and Swain used

scanning electrochemical microscopy (SECM) as well as conductive atomic force microscopy to study hydrogen-terminated boron-doped diamond electrodes with different doping levels.⁹ SECM has also been employed in our group to determine the local doping level of boron-doped polycrystalline electrodes.³⁵ Recently, Macpherson et al. used SECM in conjunction with cathodoluminescence and conducting atomic force microscopy (C-AFM) to study the impact of grain-dependent boron uptake on the electrochemical and electrical properties of polished, polycrystalline, and oxidized BDD electrodes.³⁶ Whereas C-AFM showed no evidence for enhanced grain boundary conductivity, different characteristic conductivity domains were observed corresponding to different crystallites in the diamond electrode. Using Ru(NH₃)₆³⁺ as a redox mediator, SECM detected local currents of the magnitude expected for metal-like behavior in some regions, whereas slower electron transfer was apparent in others.

In this article, we address the issue of the heterogeneity of boron doping in microcrystallite diamond films by examining the local optical and electrical characteristics using micro-Raman spectroscopy, Raman imaging, Kelvin probe microscopy (KFM), and conducting AFM (C-AFM). In particular, we used two different micro-Raman imaging techniques to investigate the chemical and structural inhomogeneities that exist in the films, at micrometer resolution. KFM, which is based on the noncontact atomic force microscopy mode, offers the possibility to obtain the sample's surface work function with a lateral resolution in the nanometer range, enabling the study of the grain boundaries in significant detail. SECM was used in an effort to estimate the doping level of the sample.

The polycrystalline diamond films studied were polished free-standing films, with a reported average boron concentration of 5×10^{20} boron atoms cm⁻³. These films are commercially available from Windsor Scientific (Slough Berkshire, U.K.) and are similar to those that were examined in ref 36.

2. Experimental Section

Materials. Potassium chloride, hydrochloric acid, and iridium chloride (IrCl₆⁻³) were purchased from Aldrich and used without further purification. Pt wire (10 μm in diameter) was obtained from Goodfellow.

Boron-Doped Diamond Films. Polycrystalline boron-doped free-standing diamond films were purchased from Windsor Scientific (Slough Berkshire, U.K.). Briefly, highly boron-doped polycrystalline CVD diamond layers were grown to a thickness greater than 500 μm by adding diborane to the methane and hydrogen source gases supplied to a microwave CVD reactor. The samples were polished on both the nucleation and growth sides to a mirror finish. The final BDD electrodes had a thickness of about 500 μm. The electrodes were supplied as 5 × 5 mm square plates. The resultant samples had a bulk electrical resistance of about 0.75 Ω m. The average solid-state boron concentration of this material was reported by the manufacturer to be about 5×10^{20} cm⁻³ as determined by secondary ion mass spectroscopy (SIMS). Prior to use, samples were cleaned in 3:1 (v/v) concentrated H₂SO₄/H₂O₂ (30%) for 15 min, rinsed copiously with Milli-Q water, and then slightly polished using diamond paste (0.3 μm) to obtain a smooth particle-free surface. Experiments were carried out on different samples with similar results.

Raman Spectroscopy. Micro-Raman scattering measurements were performed using two different spectrometers. The first was a Jobin-Yvon T64000 triple monochromator spectrometer that allowed measurements in both the visible and UV

spectral ranges. For this purpose, it was equipped with a UV-enhanced liquid-nitrogen-cooled CCD detector, a microscope, two different confocal optics, and interchangeable gratings (2400, 1800, 600 grooves/mm). A long-working-distance 50 \times (numerical aperture or NA = 0.5) objective and a UV-dedicated 40 \times (NA = 0.5) objective were used to focus the laser on the sample surface and collect the scattered light. The second spectrometer was an InVia Renishaw spectrometer that allowed measurements in the visible and near-infrared spectral ranges. It was equipped with an air-cooled CCD detector and a microscope. Spectra were acquired using a 50 \times (NA = 0.95) objective.

In the present work, samples were first examined with conventional micro-Raman spectroscopy at different excitation wavelengths. The three excitation wavelengths used were the 514-nm line of a krypton–argon laser, the 785-nm line of a laser diode, and the 244-nm line of a frequency-doubled argon laser (Coherent 90C FreD series). Although the powers of the three lasers were adjusted over a wide range during the measurements, no dramatic changes in the shape of the spectra or in the frequency and width of the diamond line were observed, indicating a high thermal conductivity of the samples. Using the acquisition conditions described above, the spectral resolution of the two different systems was $<0.1\text{ cm}^{-1}$. Samples were also examined using Raman imaging, and two different imaging techniques were employed: image reconstruction (“spectral” imaging) and direct imaging (“global” or “wide-field” imaging). For the first method, samples were mounted on XY tables. During the mapping, the full spectra for each point were recorded and stored in an image file. Images were then constructed from the information available in the individual spectra, by plotting the frequency, width, and integrated intensity of the lines as a function of the spatial coordinates. Data processing was performed using factory-supplied software (Jobin Yvon LabSpec 4.0 and Renishaw Wire 2.0).

Wide-field (or global) Raman images were obtained using the InVia Renishaw spectrometer. Here, the laser beam was defocused to illuminate a disk-shaped area on the sample, and the resulting Raman scattered light was filtered and focused to produce the image directly on the CCD detector. The tunable filters were dielectric filters with a $\sim 20\text{ cm}^{-1}$ band-pass. The sizes of the illuminated areas were about 30 and 80 μm for 50 \times and 20 \times objectives, respectively. Images were only roughly corrected for inhomogeneous laser illumination in the analyzed area. For Raman imaging, the excitation source was systematically the 514.5-nm line from an Ar⁺ laser.

Kelvin Probe Force Microscopy. Kelvin probe images were recorded under a stream of argon using a multimode model AFM (Veeco, Santa Barbara, CA) equipped with a Nanoscope IIIa controller (Digital Instruments) in the KFM-interleave mode. Single-beam silicon cantilevers coated with Pt/Ir (Arrow-EFM-50, Nanoworld) with a spring constant of $\sim 2.8\text{ N m}^{-1}$ and a resonance frequency of $\sim 75\text{ kHz}$ were used. An ac bias voltage of 2 V was applied through the tip. A lift scan height of 20–70 nm and a scan rate of 0.5 Hz were used for all experiments.

Conducting AFM. The samples were imaged with a Dimension 3100 model AFM (Veeco, Santa Barbara, CA) equipped with a Nanoscope IV controller (Digital Instruments) with a C-AFM apparatus. Platinum/iridium cantilevers (CONTPt-20 contact mode pointprobe, Nanoworld) with force constants of $\sim 0.2\text{ N m}^{-1}$ and resonant frequencies of $\sim 13\text{ kHz}$ were used (contact mode). A bias voltage was applied to the sample from the AFM controller, and the tip was at virtual ground. Current–voltage curves were recorded using a separate DAQ card (DT

306, Data Translations) and software. No current-limiting resistor was added to the circuit.

Scanning Electron Microscopy (SEM). Scanning electron microscope images were obtained using an ULTRA 55 electron microscope (Carl Zeiss, Le Pecq, France) equipped with a thermal field-emission emitter and three different detectors (an EsB detector with a filter grid, a high-efficiency In-lens SE detector, and an Everhart–Thornley secondary electron detector).

Scanning Electrochemical Microscopy (SECM). The SECM apparatus was built at LEPMI in collaboration with J. Heinze and is nearly identical to the one described in ref 37. The SECM tips were made of a Pt wire (10 μm in diameter), sealed in a glass tube. The ratio of the glass ring to the Pt disk radius (R_g) was 25. The diamond samples were studied through SECM experiments at room temperature in an aqueous solution of IrCl_6^{3-} (10 mM in 0.5 M KCl), acidified to pH 3 by addition of hydrochloric acid.

3. Results and Discussion

3.1. Morphology of the Free-Standing Polycrystalline Diamond Films. The morphology and structure of the free-standing polycrystalline diamond films were investigated using scanning electron microscopy (SEM). Figure 1a,b shows top views of one of the samples examined here, and one can clearly see structures of different dimensions down to 1 μm in size. The average apparent grain size is between 10 and 50 μm . Previous studies on boron-doped diamond have shown that secondary electron emission reaches a maximum at boron concentrations of 10^{19} – 10^{20} cm^{-3} .³⁸ Thus, the observed contrast in the SEM images arises from differences in the boron contents of the different sectors. From the contrast of the images, it seems that only two types of regions are present in the film. Similar surface morphologies can be seen using standard optical microscopy, illuminating the sample in reflection. In the latter case, the contrast between the different regions is lower, but it tends to indicate that the lighter regions correspond to domains of lower boron concentration and the darker regions to domains of higher boron concentration. The columnar structure of the film is clearly seen in the cross-sectional image (Figure 1c), where differences in the boron concentrations of the different sectors are also observed.

Current–voltage curves were recorded for dark and bright regions of the boron-doped diamond using conducting AFM (C-AFM). They were recorded in air with a dc sample bias of between +1 and –1 V. The currents were found to vary from grain to grain across the surface by about 1 order of magnitude. Figure 2 shows examples of i – E curves for two different regions on the diamond sample. They are similar in shape to those given in ref 36.

3.2. Raman Spectroscopy. Raman spectra of heavily boron-doped diamond vary continuously as their boron concentration increases.^{30,39–48} Above a doping level of about 10^{19} cm^{-3} , a first change is the downshift, asymmetrical broadening, and decrease in intensity of the diamond first-order peak. This specific line shape is often described as so-called Fano interference.⁴⁹ The Fano effect results from a quantum interference between a discrete zone center phonon and a continuum of electronic levels at the same energy. The decrease in intensity of the Raman zone center optical phonon also results from the decrease of the transmissivity of the diamond upon doping. Another specific feature of the Raman spectra of boron-doped diamond is a particularly complex spectrum that also depends

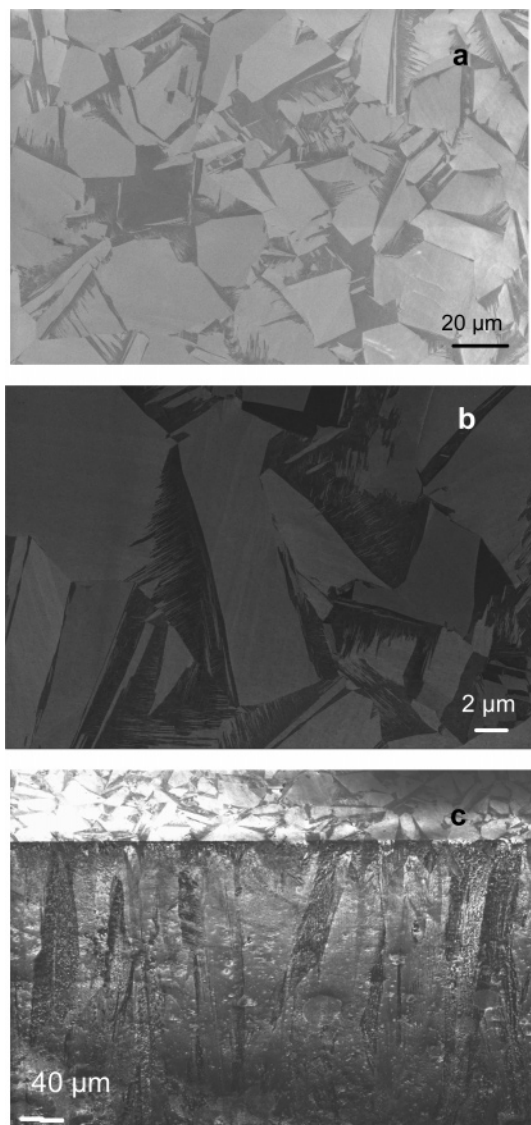


Figure 1. SEM images of the oxygen-terminated polished polycrystalline BDD interface: (a,b) top view, (c) side view.

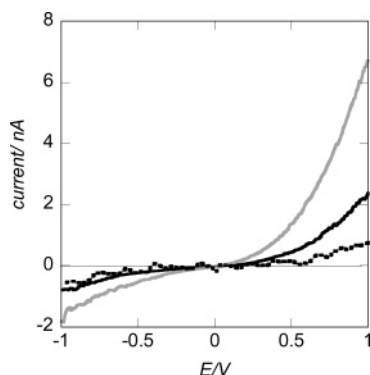


Figure 2. Current–voltage curves obtained using C-AFM for different regions on the BDD interface in air: high conductivity (gray line, dark regions in SEM image), lower conductivity (black solid and dotted lines, brighter areas in SEM image).

on the boron concentration. Broad bands centered at around 500 and 1225 cm^{-1} were observed for boron concentrations higher than ca. $3 \times 10^{20} \text{ cm}^{-3}$, whereas low-intensity signals peaking at about 610, 925, 1045, 1375, and 1470 cm^{-1} could be detected for boron concentrations in the 10^{18} – 10^{20} cm^{-3} range. It is worth mentioning that the transition between the two kinds of signals

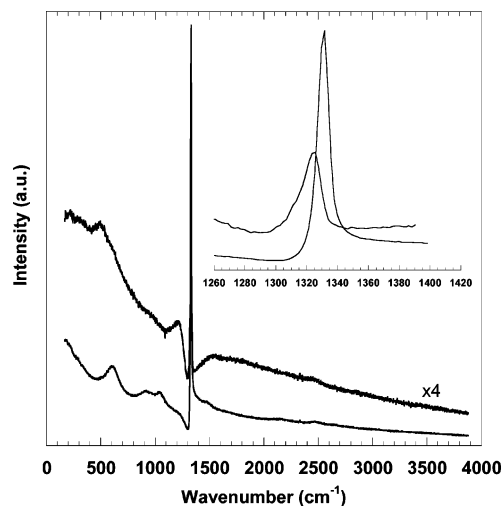


Figure 3. Micro-Raman spectra recorded in the dark (higher trace) and bright (lower trace) regions evidenced in the SEM images. Spectra are displaced vertically for clarity. The excitation wavelength was 514 nm. Inset: Magnification of the diamond line.

was observed for boron concentrations of $\sim 3 \times 10^{20} \text{ cm}^{-3}$, which is approximately where the insulator-to-metal transition is expected.^{1,50} The origin of these bands is still open to debate. The evolution of the spectra with the doping level is beyond the scope of this work. In this study, we merely employ the spectral features for relative comparisons.

The Raman analysis of the samples was conducted by keeping the spectrometer settings, such as optical alignment, laser power at the sample, and acquisition time, constant while probing different areas on the BDD, in particular, the dark and light areas observed by SEM and optical microscopy. Two different types of spectra were obtained using the 514.5-nm excitation line, depending on whether the laser was focused on the dark or bright regions. The line shapes and spectral features of these spectra are reported in Figure 3. In the bright regions, the one-phonon diamond Raman line dominates the signal. Its position is slightly downshifted ($\sim 2 \text{ cm}^{-1}$) with respect to the expected position of a reference, nominally undoped, single-crystal diamond. Also observed are low-intensity signals peaking at about 610, 925, 1045, 1375, and 1470 cm^{-1} . In the dark areas, the diamond line position was downshifted to about 10 cm^{-1} , and the line width was significantly broadened to about 17 cm^{-1} . A pronounced asymmetry of the diamond line was also observed. In addition, the broad bands centered at about 500 and 1225 cm^{-1} also accompanied a sharp diamond phonon, along with a strong increase of the low-frequency electronic scattering.

These broad lines, related to the boron doping level in the diamond, perfectly correspond to those previously observed for polycrystalline boron-doped CVD diamond films boron-doped HTHP crystals and boron-doped epilayers with similar solid-state boron concentrations. As a result, one can conclude that the polycrystalline films examined here contain a mixture of microcrystals with different boron doping levels, i.e., metallic and semiconducting diamond microcrystals. Comparing the present spectra to those obtained by our group or by others, the boron concentration can be estimated to lie in the high 10^{19} cm^{-3} range for the bright (low-boron-concentration) regions and in the high 10^{20} cm^{-3} range for the dark (high-boron-concentration) regions. This is in agreement with the SIMS results.

The spectra exhibited a considerable wavelength dependence as the incident photon energy was increased from the near-IR to the deep-UV region, as shown in Figure 4a,b. For the two

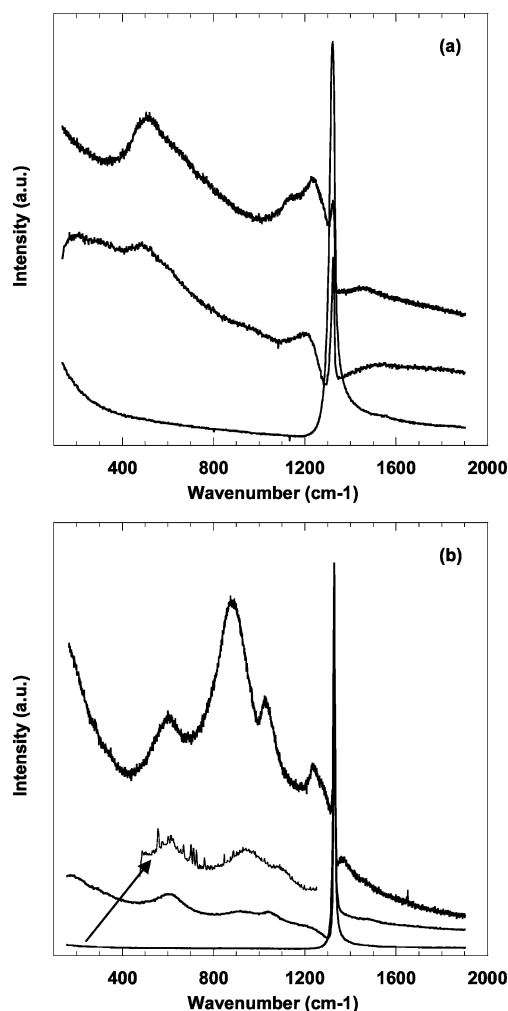


Figure 4. Evolution of the micro-Raman spectra with the excitation wavelength: (a) spectra recorded in the high-boron-concentration regions, (b) spectra recorded in the low-boron-concentration regions. The spectra were obtained at (bottom) 244, (middle) 514, and (top) 785 nm. The inset is a magnification of the baseline of the spectrum obtained at 244 nm.

types of spectra, a strong decrease of the electronic scattering continuum and of the boron-related signals tuning the excitation wavelength from the near-IR to the deep-UV was observed. In particular, the broad bands seen in the metallic parts of the samples disappeared, whereas the 610, 925, and 1045 cm^{-1} bands observed in the semiconducting regions could be observed only after a strong magnification of the intensity scale. Other differences can be observed by comparing the spectra obtained with visible and near-IR excitations. First, there is a strong decrease of the diamond line intensity, as compared to the intensities of the broad signals and the electronic scattering background. Second, some modifications in the structure of the broad signals are observed. For both the semiconducting and metallic regions, different lines are clearly resolved in the 1000–1300 cm^{-1} range, and a broad band peaking at about 900 cm^{-1} is observed in the spectra, both of which are characteristic of semiconducting microcrystals (see Figure 4b).

Figure 5a,b shows magnified spectra to clearly present the line shape of the diamond line. In all cases, the diamond line is downshifted from the expected position of a reference single-crystal diamond. However, the dependence of the frequency of the diamond line on the excitation wavelength seems weak: Downshifts of ~ 2 and $\sim 10 \text{ cm}^{-1}$ are still observed for the low- and high-conductivity regions, respectively, regardless of the

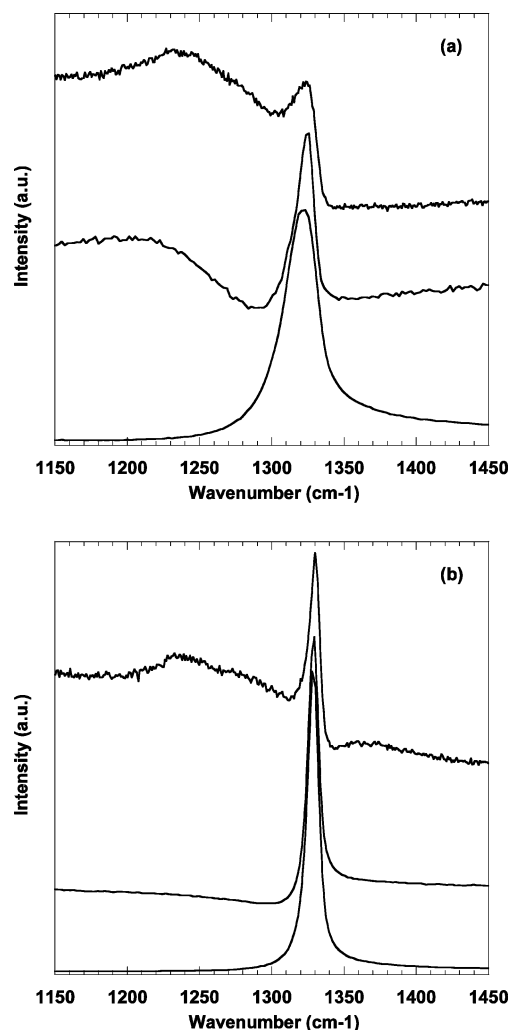


Figure 5. Evolution of the line profile of the diamond line with the excitation wavelength. Same spectra as in Figure 4. The intensity scale of each spectrum was adjusted to clearly present the diamond line profile.

excitation wavelength. A strong broadening of the line is still observed for the metallic regions, despite the difficulties involved in comparing the absolute values because of the setup and wavelength-dependent instrumental broadening. Whatever the excitation wavelength, the diamond line was found to be more or less asymmetric. In most cases, the diamond line exhibits a tail on the low-wavenumber side that increases with the boron content. Moreover, for 514- and 244-nm excitations, the baseline also exhibits a strong asymmetry, with a dip on the low-wavenumber side of the phonon Raman peak. Finally, strong intensity variations are observed between the spectra of the different regions. Qualitatively, the differences in response between the different regions are also wavelength-dependent, and the largest intensity differences are observed using the 244-nm line.

3.3. Spectral Raman Imaging. An optical image of one of the samples examined in this work is presented in Figure 6. In the center of this image is a $120 \times 96 \mu\text{m}^2$ region (highlighted in the box) that indicates where the Raman data were acquired. An objective lens of low magnification ($50\times$) was used, and because of the low numerical aperture ($\text{NA} = 0.5$), the probing depth was high and was mostly governed by the optical properties of the sample. Spectra were acquired with a $1\text{-}\mu\text{m}$ spacing using an acquisition time of 2 s per spectrum. A 600 grooves mm^{-1} grating was used in combination with a notch

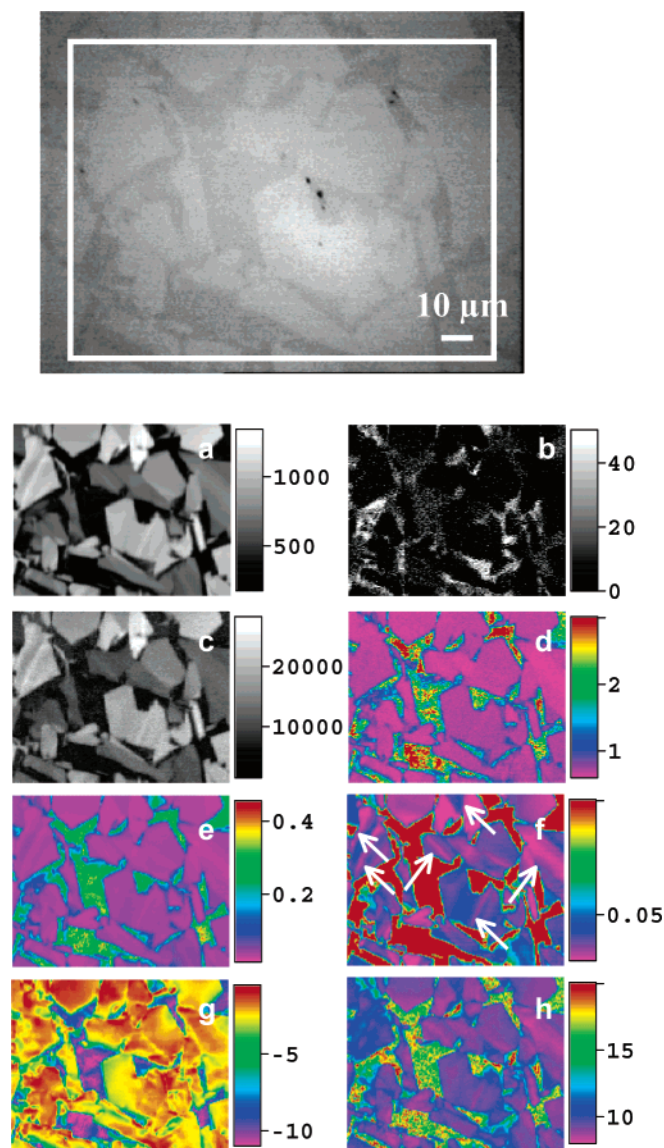


Figure 6. Optical (sample illuminated in reflection) and Raman images of the CVD boron-doped diamond film (the rectangle indicates the analyzed area): (a) integrated diamond line intensity at 1332 cm^{-1} ; (b) integrated intensity at $\sim 1550\text{ cm}^{-1}$ associated with the presence of amorphous carbon; (c) integrated line intensity at ~ 500 or 610 cm^{-1} associated with the boron dopant atoms; (d) the same image as c but normalized to the diamond line intensity; (e) integrated intensity of the electronic scattering background, measured at $\sim 300\text{ cm}^{-1}$ and normalized to the diamond line intensity; (f) same as e at magnified intensity scale; (g) diamond line position as a shift from 1332 cm^{-1} ; and (h) diamond line width.

filter to reject Rayleigh scattering. Under these conditions, the $200\text{--}2200\text{ cm}^{-1}$ range can be investigated within a single acquisition. As a consequence of the low-dispersion conditions, the full width at half-maximum of a reference single-crystal diamond was 5.8 cm^{-1} .

Figure 6 shows a series of spectral maps including (a) the integrated diamond line intensity at 1332 cm^{-1} , (b) the integrated intensity at 1550 cm^{-1} associated with the presence of amorphous carbon,⁵¹ (c) the integrated line intensity of the 500 and 610 cm^{-1} bands associated with the boron dopant atoms ($I_{500-610}$ map), (d) the $I_{500-610}/I_{1332}$ ratio, (e) the integrated intensity of the electronic scattering background measured at about 300 cm^{-1} normalized to the diamond line intensity, (f) the same as e at magnified intensity scale, (g) the diamond line position as a shift from 1332 cm^{-1} , and (h) the diamond line width.

One can observe that the intensity map of the diamond line correlates well with the optical image: It is possible to identify all of the individual crystallites. The similarity of the diamond line intensity and the optical images was a reproducible feature that was found for all of the different areas of the sample that were examined. Two types of regions are present that are identified by the two types of spectra described above. The line intensity varies by over a factor of 15 between the dark regions (high boron concentration) and the bright ones (low boron concentration). Intensity variations are observed within regions of both low and high boron concentration, reflecting nonhomogeneous boron concentrations within the individual grains. Note that higher intensity variations are observed within the high-concentration regions. Because no explicit polarization analysis was performed, the intensity of the Raman line in backscattering is also expected to be a strong function of the angle between the *E* vector of the incident laser and the in-plane orientation of the crystal. Because the laser is linearly polarized and the diffraction gratings used in the spectrometer have strong polarization dependence, intensity variations are also expected to depend on the orientation of the crystals with respect to the incoming beam. The polarization dependence of the diamond line intensity can partially explain the intensity contrast observed in Figure 6a.

Interestingly, there is a clear difference in the Raman signal between the regions of low and high boron concentration, which indicates that the spatial resolution is a fraction of a micrometer: It has been observed that recorded spectra separated by $1\text{ }\mu\text{m}$ did not interfere. In contrast to what was observed for similar polished boron-doped diamond films with lower average boron contents, however, no specific Raman or photoluminescence signal was detected within the grain boundaries.

Figure 6b shows that the electrodes contained some amorphous carbon, as evidenced by a broad signal centered at about 1550 cm^{-1} . The amorphous carbon was mostly detected in the regions of high boron concentration. This was also a reproducible feature that was observed for different areas of the sample. However, it is not possible to give any quantitative information about the amount of amorphous carbon present in the high-boron-concentration regions. This would require knowledge of the optical constants and grain size of the amorphous carbon clusters.

The intensity of both the 500 and 610 cm^{-1} lines was high enough that it could be fitted by a mixed Gaussian–Lorentzian line shape. In particular, the image that was constructed from the intensity of these lines (Figure 6c) is similar to the diamond line intensity image: Again, all of the crystallites are identified. The variations in this boron-related signal intensity are nicely visualized in the $I_{500-610}/I_{1332}$ map (Figure 6d). These plots tend to indicate that there are no apparent variations in the intensity of the boron-related signal within the regions of low boron concentration. In the low-boron-doped areas, the ratio of the integrated intensity at about 610 cm^{-1} remains constant to within approximately 10%, whereas in the higher-boron-doped regions, the same ratio can vary by about a factor of 5. The intensity of the electronic Raman scattering was also used to construct the images shown in Figure 6e,f. The intensity of the electronic scattering was normalized to the diamond line intensity. Again, the image reveals all of the crystallites, with a contrast that is similar to that of the normalized $500\text{--}610\text{ cm}^{-1}$ intensity image. However, at magnified intensity scale, some details in the individual grains are revealed (arrows in Figure 6f). The features likely correspond to twins within the individual crystallites. These details are not observed in the previous image. Again,

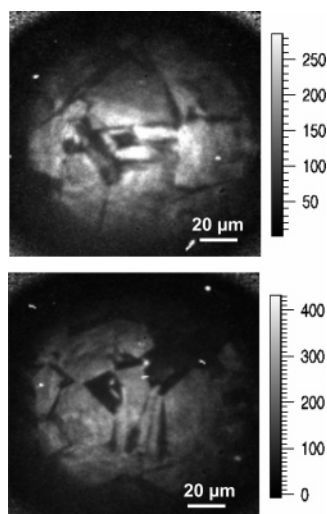


Figure 7. Examples of wide-field Raman images. The dielectric filter was centered at the diamond line frequency (1332 cm^{-1}).

higher intensity variations are still observed within the high-concentration regions, reflecting a nonhomogeneous boron concentration.

Finally, the diamond line frequency and width of the images are given in Figure 6g and h, respectively. The individual crystallites are again identified in both images. For doping levels higher than 10^{19} cm^{-3} , the frequency and width of the diamond line are known to be affected by the boron content and, thus, to reflect the boron concentration to some extent. The low- and high-concentration regions are readily identified on both images, with average downshifts of about 2 cm^{-1} for the low-concentration regions and about 10 cm^{-1} for the high-concentration regions. However, the frequency and width of the diamond line also depend of the amount of strain that is present in the individual crystallites, making it difficult to use these images to quantify the boron content in the individual crystallites. Strain in such CVD films is known to be accompanied by line splitting. Line splitting, which reflects the loss of perfect cubic symmetry, was rarely observed during the analysis of this sample, which is a strong indication that the strain level in these polycrystalline samples was generally low. A close examination of Figure 6h shows that most of the details evidenced in Figure 6f are reproduced: In some sectors, the small line width variations correspond to small differences in boron concentration. Similar images were recorded using higher-dispersion conditions, and similar results were obtained.

3.4. Wide-Field Raman Imaging. A second method of Raman imaging, via global (wide-field) illumination, was applied to study the boron-doped CVD samples. This imaging technique does not record a Raman spectrum but instead provides an image of the spatial distribution of the light corresponding to a narrow spectral range. The spectral resolution is low ($\sim 20\text{ cm}^{-1}$), and the resulting signal results from all of the light collected through the filter, including both the Raman and background signals. Of course, the information regarding the frequency and width of the diamond line is lost, but the method allows for a rapid survey of the sample. Here, a $50\times$ objective was used, giving a 500 nm/pixel resolution on the CCD. Examples of images, obtained with a 600-s collection time, are shown in Figure 7. The individual crystallites are clearly revealed despite the nonhomogeneous illumination of the sample. The intensity of the signal varies by about a factor of 5 over the examined area. Approximately the same “intensity contrast” can be obtained using spectral imaging techniques,

providing that the integrated intensity signal takes into account the electronic scattering background that is present below the diamond Raman signal. Again, this intensity contrast is mostly due to the different boron contents of the individual crystallites, with the regions of high boron concentration being dark and the regions of low boron concentration being bright.

3.5. Determination of the Doping Level Using SECM.

SECM was used as an effort to determine the boron concentrations of the different microcrystals as found using Raman imaging. SECM is based on the principle that, within a tip–substrate distance (d) of a few tip radii, the tip current changes as a function of distance in a way that is characteristic of the electrochemical reactivity of the diamond surface. A negative feedback (the tip current decreases when the tip–substrate distance decreases, as diffusion of IrCl_6^{2-} to the tip electrode is blocked) is observed if the diamond film is behaving as an insulator, whereas a positive feedback is expected for highly doped diamond electrodes (Figure 8). The SECM approach is based on a previous report by us in which polycrystalline diamond electrodes of different doping levels were investigated.³⁵ The redox couple chosen to determine the doping level of the BDD sample was $\text{IrCl}_6^{2-}/^{3-}$, an outer-sphere redox couple. In this case, a simple electron transfer on diamond is observed for which the electrochemical reaction rate is insensitive to the surface termination but is sensitive to the energetic positions of its surface conduction and valence band edges versus the most-probable electron energy levels of the oxidized and reduced form of the used redox couple and also to the densities of vacant and occupied electron energy states at the surface band edges, which depend on the applied potential and, of course, on the dopant concentration. Considering the range of flatband potential values found in the literature for BDD ($E_{\text{FB}} \approx 0.4\text{--}1.6\text{ V vs Ag/AgCl}$),^{1,52–55} $\text{IrCl}_6^{2-}/^{3-}$ is the ideal candidate for these investigations. The diamond samples were thus studied by SECM experiments at room temperature in an aqueous solution of IrCl_6^{3-} (10 mM in 0.5 M KCl), acidified to pH 3 by addition of hydrochloric acid. The approach curve, determined by measuring the change in tip current (i_T) as the tip approaches the diamond surface, was recorded by polarizing the platinum microelectrode at a potential ($E_{\text{tip}} = 1.1\text{ V vs Ag/AgCl}$) chosen to oxidize IrCl_6^{3-} to IrCl_6^{2-} under steady-state conditions. The potential applied on the BDD interface varied between $E_F = -0.30$ and $E_F = +0.55\text{ V vs Ag/AgCl}$. Figure 8 shows approach curves for different regions on the BDD sample. These different approach curves were obtained by approaching, stepwise, different areas on the BDD sample (scanned distance: $300\text{ }\mu\text{m}$ in $20\text{-}\mu\text{m}$ steps). The curves presented in Figure 8A,B indicate the upper and lower limits found and are suggested to correspond to the dark (Figure 8A) and bright (Figure 8B) regions in the SEM and optical images. Pure positive feedbacks independent of the bias of the diamond sample were obtained for the dark regions of the BDD samples, showing that these parts of the diamond samples have a metallic character. The boron concentration of these zones is higher than $\sim 3.0 \times 10^{20}\text{ cm}^{-3}$, the boron concentration at which the Mott transition occurs.⁵⁶ Different electrochemical behavior was recorded for the bright regions (Figure 8B). The shape of the approach curves depends on the applied potential, a characteristic of semiconductor interfaces.³⁵ Indeed, at a selected potential of $E_F = 0.5\text{ V vs Ag/AgCl}$ applied to the diamond interface, the recorded feedback currents showed a lesser amount of positive feedback. The experimental SECM approach curves can be fitted to theoretical approach curves using the theory of a kinetically controlled i_T – d curve at a completely conductive surface where

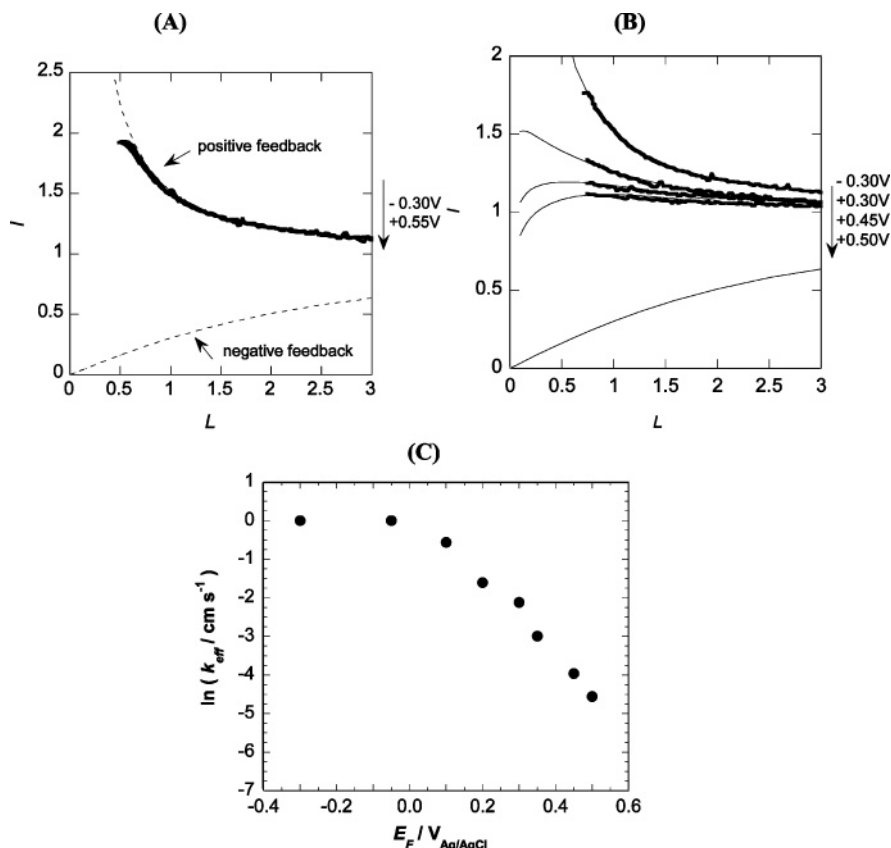


Figure 8. Approach curves for the boron-doped diamond surface in two different areas: (A) highly doped, (B) lower doped. Bold lines, experimental curves; thin lines, fitted curves. Experimental conditions: IrCl_6^{3-} (10 mM) in 0.1 M KH_2PO_4 (pH 3), $E_{\text{tip}} = 1.1$ V vs Ag/AgCl, $E_F = -0.30$ to 0.55 V vs Ag/AgCl. (C) Plot of $\ln k_{\text{eff}}$ as a function of applied potential E_F (low-doped regions).

the heterogeneous kinetics is finite.⁵⁷ By decreasing the potential applied to the BDD interface and recording the approach curves, the heterogeneous rate constants at the diamond electrode, k_{eff} , as a function of potential, E_F , could be calculated. Fitting of these data using the theory of electron transfer at semiconductor/electrolyte interfaces was not possible, as the areas were still too highly doped.³⁵ An almost linear relationship between k_{eff} and E_F is observed. However, by comparing the results with our previous investigations,³⁵ we can estimate that the carrier density in these microcrystals is above $\sim 8 \times 10^{19} \text{ cm}^{-3}$ and below $\sim 3.0 \times 10^{20} \text{ cm}^{-3}$. This result is in agreement with those obtained from Raman spectroscopy, where it was found that the bright and thus lower-doped regions have a boron concentration in the high 10^{19} cm^{-3} range.

3.6. Kelvin Probe Force Microscopy. Kelvin probe force microscopy not only allows for the determination of the surface topography, as does atomic force microscopy, but also provides images of the surface work function on the nanometer scale depending on the shape and diameter of the probe tip.⁵⁸ Here, Kelvin probe force microscopy (KFM) was first used to determine whether the electronic properties of the BDD sample change significantly at the grain boundaries. As the surface electronic properties have been shown to be strongly affected by atmospheric adsorption,²⁵ KFM experiments were performed under argon. Figures 9a and 10a show typical topographic tapping-mode AFM images of an oxidized polished BDD interface. The high quality of the polish is demonstrated by the root-mean-square roughness of approximately 1 nm. Nevertheless, it is still possible to differentiate some surface features in the topographic image. In both images, some grain boundaries can be distinguished. Moreover, more features are seen in particular in the right part of Figure 10a. A reason that the AFM

images show these features could be that different surface facets polish at different rates; therefore, there are small height differences on the sample that can be picked out. Finally, the particle observed in the lower part of the AFM image in Figure 9a corresponds to an impurity on the surface. Indeed, it was observed that the oxygen-terminated BDD electrode readily adsorbed impurities onto its surface, most likely because of its hydrophilic character.

The corresponding KFM images in Figures 9b and 10b were recorded under argon with a tip–BDD sample distance of 50 nm and a sample bias ac voltage of 2 V. For both images, the surface potential varied by about 20 mV across the scanned area. A small contact potential difference was observed on the two sides of some of the grain boundaries that revealed different crystalline domains. However, the grain boundaries themselves did not exhibit any specific contrast. From Figure 10b, it can be observed that polishing of the BDD surface might leave species adsorbed on the surface as revealed in the KFM image.

A gold layer was used for calibration of the KFM measurements. A constant surface potential of about 20 mV was obtained for these reference gold films scanned under the same conditions. Thus, the work functions of gold and oxygenated boron-doped diamond are almost identical. The gold reference work function is known to be 4.9 ± 0.1 eV below the vacuum level.⁵⁹ The fluctuations that can be seen in the KFM images are about 0.02 eV. With respect to 4.9 eV, these fluctuations are considered to be negligibly small and might be due either to fluctuations in dopant concentration or to the presence of a nonhomogeneous adsorption layer. However, these results are rather preliminary. Indeed, it is difficult to extract quantitative information for the KFM images, and we are undertaking on a more detailed study of this problem. KFM has, however, already

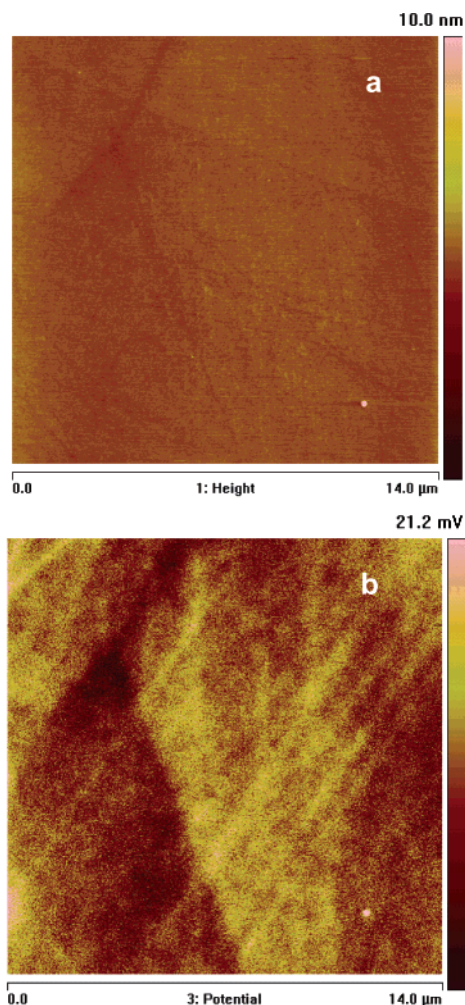


Figure 9. (a) Tapping-mode AFM image of an oxygen-terminated polished polycrystalline BDD surface, (b) KFM surface potential image of the same surface area.

proven to be useful for both the observation of well-characterized grain boundaries in polycrystalline silicon⁶⁰ and the characterization of CuGaSe₂ films,⁶¹ and we expect that this technique is sensitive enough to resolve boron accumulation.

4. Conclusion

The issue of the heterogeneity of boron doping in microcrystalline diamond films was addressed by four different methods: micro-Raman spectroscopy and Raman imaging, Kelvin probe force microscopy, conducting AFM, and SECM. Two of these techniques, micro-Raman spectroscopy and SECM, were used to estimate the local boron concentration within individual crystallites. The samples were commercially available films from Windsor Scientific, with an average boron concentration of about $5 \times 10^{20} \text{ cm}^{-3}$.

In agreement with previous works, all of the methods showed that the boron uptake is nonuniform across the surface of the electrode. Two different types of regions, with metallic or semiconducting properties, were identified through their Raman spectral features. The line shape of these spectra is strongly dependent on the excitation wavelength. By comparing our results with those in the literature, the boron concentration can be estimated to lie in the high 10^{19} cm^{-3} range for the semiconducting regions and in the high 10^{20} cm^{-3} range for the metallic regions. Local variations in electroactivity were observed from the SECM approach curves, which are related

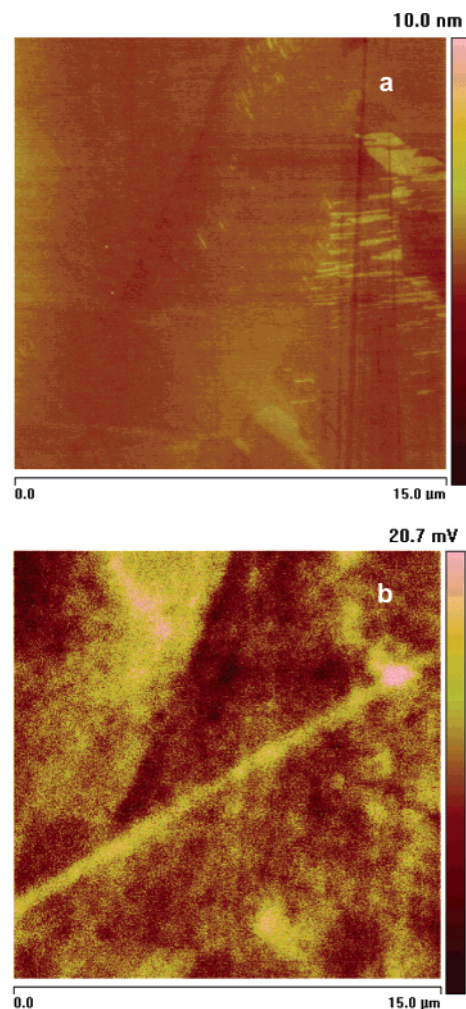


Figure 10. (a) Tapping-mode AFM image of an oxygen-terminated polished polycrystalline BDD surface, (b) KFM surface potential image of the same surface area.

to the electronic properties of the individual grains, which, in turn, are governed by the boron content of the individual crystallites.

Micro-Raman spectroscopy, when used with appropriate mapping stages, is an efficient tool for characterizing samples that present heterogeneities at the micrometer scale. In this study, two different imaging techniques were used that revealed the grain structure of the films: Images constructed from the diamond line intensity perfectly reproduced the optical images obtained by illuminating the sample in reflection. The method also allows the detection of the presence of nondiamond carbon, especially in the metallic parts of the samples. Other spectral features (intensity of the boron-related broad lines and frequency and width of the diamond line) were also used to construct images. In every case, the grain structure of the film was revealed, as well as twinning within individual crystallites. It is worth noting that the quality of the Raman images now compares to that of more typical SEM or cathodoluminescence images.³⁶

Finally, in agreement with ref 36, all approaches revealed that no enhanced doping or boron depletion at the grain boundaries. Using SECM, the carrier density in the low-doped regions could be estimated and was found to be above $\sim 8 \times 10^{19} \text{ cm}^{-3}$ and below $\sim 3.0 \times 10^{20} \text{ cm}^{-3}$. Despite the uncertainty introduced by the preparation of the sample, Kelvin force probe microscopy supports the conclusion that there is nothing specific at the grain boundaries. In this way, the electrochemical behavior

of these electrodes seems different from that of the lower-doped samples examined in ref 9, for which the strongest electrochemical activity was evidenced at the grain boundaries.

Acknowledgment. The Centre National de la Recherche Scientifique (CNRS) and the Nord-Pas-de Calais region are gratefully acknowledged for financial support.

References and Notes

- (1) Granger, M. C.; Witek, M.; Xu, J.; Wang, J.; Hupert, M.; Hanks, A.; Koppang, M. D.; Butler, J. E.; Lucazeau, G.; Mermoux, M.; Strojek, J. W.; Swain, G. M. *Anal. Chem.* **2000**, *72*, 3793.
- (2) Tryk, D. A.; Tsunozaki, K.; Rao, T. N.; Fujishima, A. *Diamond Relat. Mater.* **2001**, *10*, 1804.
- (3) Compton, R. G.; Foord, J. S.; Marke, F. *Electroanalysis* **2003**, *15*, 1349.
- (4) Troster, I.; Fryda, M.; Hermann, Schafer, L.; Hanni, W.; Perret, A.; Blaschke, M.; Kraft, A.; Stadelmann, M. *Diamond Relat. Mater.* **2002**, *11*, 640.
- (5) Yang, W.; Butler, J. E.; Russell, J. N.; Hamers, R. J. *Langmuir* **2004**, *20*, 6778.
- (6) Lasseter, T. L.; Clare, B. H.; Abbott, N. L.; Hamers, R. J. *J. Am. Chem. Soc.* **2004**, *126*, 10220.
- (7) Zhang, G.-J.; Song, K.-S.; Nakamura, Y.; Ueno, T.; Funatsu, T.; Ohdomari, I.; Kawarada, H. *Langmuir* **2006**, *22*, 3728.
- (8) Carlisle, J. A. *Nature Mater.* **2004**, *3*, 668.
- (9) Holt, K. B.; Bard, A. J.; Show, Y.; Swain, G. M. *J. Phys. Chem. B* **2004**, *108*, 15117.
- (10) Werner, M.; Job, R.; Zaitzev, A.; FAhrner, W. R.; Seifert, W.; Johnston, C.; Chalker, P. R. *Phys. Status Solidi A* **1996**, *154*, 385.
- (11) Foord, J. S.; Hian, L. C.; Jackman, R. B. *Diamond Relat. Mater.* **2001**, *10*, 710.
- (12) Notsu, H.; Yagi, I.; Tatsuma, T.; Tryk, D. A.; Fujishima, A. *J. Electroanal. Chem.* **2000**, *492*, 31.
- (13) Shirafuji, J.; Sugino, T. *Diamond Relat. Mater.* **1996**, *5*, 706.
- (14) Foord, J. S.; Lau, C. H.; Hiramatsu, M.; Jackman, R. B.; Nebel, C. E.; Bergonzo, P. *Diamond Relat. Mater.* **2002**, *11*, 856.
- (15) Saby, C.; Muret, P. *Diamond Relat. Mater.* **2002**, *11*, 851.
- (16) Ando, T.; Yamamoto, K.; Ishii, M.; Kamo, M.; Sato, Y. *J. Chem. Soc., Faraday Trans.* **1993**, *89*, 3635.
- (17) Pehrsson, P. E.; Mercer, T. W. *Surf. Sci.* **2000**, *460*, 49.
- (18) Notsu, H.; Yagi, I.; Tatsuma, T.; Tryk, D. A.; F. A., *Electrochem. Solid State Lett.* **1999**, *2*, 522.
- (19) Yagi, I.; Notsu, H.; Kondo, T.; Tryk, D. A.; Fujishima, A. *J. Electroanal. Chem.* **1999**, *473*, 173.
- (20) Boukherroub, R.; Wallart, X.; Szunerits, S.; Marcus, B.; Bouvier, P.; Mermoux, M. *Electrochem. Commun.* **2005**, *7*, 937.
- (21) Goeting, C. H.; Marken, F.; Gutiérrez-Sosa, A.; Compton, R. C. *Diamond Relat. Mater.* **2000**, *9*, 390.
- (22) Fortin, E.; Chane-Tune, J.; Mailley, P.; Szunerits, S.; Marcus, B.; Petit, J.-P.; Mermoux, M.; Vieil, E. *Bioelectrochemistry* **2004**, *63*, 303.
- (23) Notsu, H.; Fukazawa, T.; Tatsuma, T.; Tryk, D. A.; Fujiwara, Y.; *Electrochem. Solid-State Lett.* **2001**, *4*, H1.
- (24) Delabougli, D.; Marcus, B.; Mermoux, M.; Bouvier, P.; Chane-Tune, J.; Petit, J.-P.; Mailley, P.; Livache, T. *Chem. Commun.* **2003**, 2698.
- (25) Maier, F.; Ridler, M.; Mantel, B.; Ristein, J.; Ley, L. *Phys. Rev. Lett.* **2000**, *85*, 3472.
- (26) Yagi, I.; Notsu, H.; Kondo, T.; Tryk, D. A.; Fujishima, A. *J. Electroanal. Chem.* **1999**, *473*, 173.
- (27) Bennett, J. A.; Wang, J. A.; Show, Y.; Swain, G. M. *J. Electrochem. Soc.* **2004**, *151*, E306.
- (28) Janssen, G.; van Enckevort, W. J. P.; Villenberg, W.; Giling, L. J. *Diamond Relat. Mater.* **1992**, *1*, 789.
- (29) Samlenski, R.; Haug, C.; Brenn, R.; Wild, C.; Locher, R.; Koidl, P. *Diamond Relat. Mater.* **1996**, *5*, 947.
- (30) Honda, K.; Noda, T.; Yoshimura, M.; Nakagawa, K.; Fujishima, A. *J. Phys. Chem. B* **2004**, *108*, 16117.
- (31) Mermoux, M.; Marcus, B.; Swain, G. M.; Butler, J. E. *J. Chem. Phys. B* **2002**, *106*, 10816.
- (32) Steeds, J. W.; Gilmore, A.; Charles, S.; Heard, P.; Howarth, B.; Butler, J. E. *Acta Mater.* **1999**, *47*, 4025.
- (33) Charles, S. J.; Steeds, J. W.; Evans, D. J. F.; Butler, J. E. *Mater. Lett.* **2003**, *57*, 3690.
- (34) Steeds, J. W.; Mora, A. E.; Butler, J. E.; Bussmann, K. M. *Philos. Mag. A* **2002**, *82*, 1741.
- (35) Chane-Tune, J.; Petit, J.-P.; Szunerits, S.; Bouvier, P.; Delabougli, D.; Marcus, B.; Mermoux, M. *ChemPhysChem* **2006**, *7*, 89.
- (36) Wilson, N. R.; Clewes, S. L.; Newton, M. E.; Unwin, P. R.; Macpherson, J. V. *J. Phys. Chem. B* **2006**, *110*, 5639.
- (37) Borgwarth, K.; Ricken, C.; Ebling, D. G.; Heinze, J. *Ber. Bunsen-Ges. Phys. Chem.* **1995**, *99*, 1421.
- (38) Miller, J. B.; Brandes, G. R. *J. Appl. Phys.* **1997**, 4538.
- (39) Ager, J. W.; Walukiewicz, W.; McCluskey, M.; Plano, M. A.; Landstrass, M. I. *Appl. Phys. Lett.* **1995**, *66*, 616.
- (40) Gonon, P.; Gheeraert, E.; Deneuville, A.; Abello, L.; Lucazeau, G. *J. Appl. Phys.* **1995**, *78*, 7059.
- (41) Locher, R.; Wagner, J.; Fuchs, F.; Maier, M.; Gonon, P.; Koidl, P. *Diamond Relat. Mater.* **1995**, *4*, 678.
- (42) Shiomi, H.; Kirillov, D.; Hagstrom, S. B. *Mater. Res. Soc. Symp. Proc.* **1993**, *283*, 897.
- (43) Ushizawa, K.; Nishitani-Gamo, M.; Watanabe, K.; Sakaguchi, I.; Sato, Y.; Ando, T. *J. Raman Spectrosc.* **1999**, *30*, 957.
- (44) Ushizawa, K.; Watanabe, K.; Ando, T.; Sakaguchi, I.; Nishitani-Gamo, M.; Sato, Y.; Kanda, H. *Diamond Relat. Mater.* **1998**, *7*, 1719.
- (45) Mermoux, M.; Marcus, B.; Swain, G. M.; Butler, J. E. *J. Chem. Phys. B* **2002**, *106*, 10816.
- (46) Pruvost, F.; Bustarret, E.; Deneuville, A. *Diamond Relat. Mater.* **2000**, *9*, 295.
- (47) Pruvost, F.; Deneuville, A. *Diamond Relat. Mater.* **2001**, *10*, 531.
- (48) Wang, Y.; Li, H.; Zhangda, Z.; Feng, K. *Jpn. J. Appl. Phys.* **2000**, *39*, 2795.
- (49) Abstreiter, G.; Cardona, M.; Pinczuck, G. In *Topics in Applied Physics. Light Scattering in Solids*; Cardona, M., Guntherholdt, G., Ed.; Springer: New York, 1984; Vol. 54.
- (50) Bustarret, E.; Gheeraert, E.; Watanabe, K. *Phys. Status Solidi A* **2003**, *199*, 9.
- (51) Mermoux, M.; Marcus, B.; Swain, G. M.; Butler, J. E. *J. Chem. Phys. B* **2002**, *106*, 10816.
- (52) Ferreira, N. G.; Silva, L. L. G.; Corat, E. J.; Trava-Airoldi, V. J. *Diamond Relat. Mater.* **2002**, *11*, 1523.
- (53) Pleskov, Y. V. *Russ. J. Electrochem.* **2002**, *38*, 1275.
- (54) Tada, K.; Sonoda, T.; Yokota, Y.; Kobashi, K.; Yoshino, K. *J. Appl. Phys.* **1998**, *84*, 5635.
- (55) Tse, K.-Y.; Nichols, B. M.; Yang, W.; Butler, J. E.; Russell, J. N.; Hamers, R. J. *J. Phys. Chem. B* **2005**, *109*, 8523.
- (56) Bustarret, E.; Gheeraert, E.; Watanabe, K. *Phys. Status Solidi A* **2003**, *199*, 9.
- (57) M. M. V.; H. B. R., *Anal. Chim. Acta* **2000**, *406*, 119.
- (58) Jacobs, H. O.; Leuchtmann, P.; Homan, O. J.; Stemmer, A. *J. Appl. Phys.* **1998**, *84*, 1168.
- (59) Rezek, B.; Sauerer, C.; Nebel, C. E.; Stutzmann, M.; Ristein, J.; Ley, L.; Snidero, E.; Bergonzo, P. *Appl. Phys. Lett.* **2003**, *82*, 2266.
- (60) Tsurekawa, S.; Kido, K.; Watanabe, T. *Philos. Mag. A* **2005**, *85*, 41.
- (61) Sadewasser, S.; Glatzel, T.; Schuler, S.; Nishiwaki, S.; Kaigawa, R.; Lux-Steiner, M. C. *Thin Solid Films* **2003**, *431–432*, 257.